High Kinetic Inductance NbN Nanowire Superinductors

David Niepce,* Jonathan Burnett, and Jonas Bylander
Microtechnology and Nanoscience, Chalmers University of Technology, Gothenburg SE-41296, Sweden

(Received 6 February 2018; revised manuscript received 22 December 2018; published 4 April 2019)

We demonstrate that a high kinetic inductance disordered-superconductor nanowire can realize a circuit element – known as a superinductor – with a characteristic impedance greater than the quantum resistance ($R_Q = h/4e^2 \simeq 6.5$ kΩ) and a quality factor of 25 000 at single-photon excitation. By examining loss rates, we demonstrate that the microwave dissipation can be fully understood in the framework of two-level-system dielectric loss. Superinductors can suppress the quantum fluctuations of charge in a circuit, which has applications, for example, in devices for quantum computing, photon detection, and other sensors based on mesoscopic circuits.

DOI: 10.1103/PhysRevApplied.11.044014

I. INTRODUCTION

Disorder within superconductors can reveal nontrivial electrodynamics [1–3], dual Josephson effects [4], and superconducting-insulating phase transitions [5]. In general, disorder increases the normal-state resistance of the superconductor, which also enhances the kinetic inductance due to the inertia of the charge carriers (the Cooper pairs).

High kinetic inductance can be used to design circuits with characteristic impedances exceeding the quantum resistance ($R_Q = h/4e^2 \simeq 6.5$ kΩ). A quantum circuit element with zero dc resistance, low microwave losses, and a characteristic impedance above R_Q is known as a superinductor [6,7]. The fluxonium qubit, based on superinductors, is immune to charge fluctuations [8] and has demonstrated extraordinary relaxation times [9]; it also has a much greater anharmonicity than the predominantly used superconducting qubits, thereby facilitating the high-fidelity quantum gate operations required for quantum computing. However, these examples of superinductors have been based on the kinetic inductance of Josephson junction arrays (JJA), and not on disordered materials, which places constraints on the possible device parameters and geometries.

An attractive alternative to JJAs is offered by the high kinetic inductance of nanowires made of strongly disordered superconducting thin films [10]. Such a superinductor should possess tremendous magnetic field tolerance, suitable for hybrid qubits, which operate at high magnetic fields [11,12]. It also exhibits an increased coupling between photons and charge, due to the enhanced zero-point fluctuations of the electric field afforded by the high impedance [12,13]. High-impedance resonators have enabled strong coupling between microwave photons and the charge in semiconductor quantum dots [14,15] and could enable strong coupling to spins [16]; superinductors should increase these effects even more. High-impedance circuits can also be used in photon detectors [17] or in mesoscopic-transport experiments, e.g., for metrology applications [18]. Additionally, nanowire-based superinductors have a wide parameter space to suppress self-resonant modes [6], which are an obstacle for demonstrating some topologically protected qubit designs [10,19].

A superconducting nanowire-based approach was previously overlooked, because a variety of circuits fabricated with strongly disordered superconductors were found to exhibit significant internal dissipation [20–23], with quality factors of 500 to 1000. There is clear experimental evidence of the existence of a disorder-related loss [24] and recent theoretical work attributes these losses to the presence of low-lying subgap states in the proximity of the superconducting-insulating transition [25].

However, it has recently been shown that it is possible to fabricate superconducting nanowires embedded within resonators that do not exhibit high dissipation [26]. In addition, 100-nm-wide resonators made from weakly disordered superconductors have also shown high-quality factors at the relatively high temperature of 280 mK and approximately 1000-photon population [13]. This motivates the need to fabricate a sufficiently disordered superconductor to obtain high inductance, but not so disordered as to induce dissipation, where the requirements can be balanced by using moderately thin films. Therefore, to maximize the characteristic impedance, it becomes crucial to minimize the stray capacitance, which can be achieved with a nanowire geometry. However, the nanowire geometry is itself more susceptible to parasitic two-level systems (TLS) compared to wider conductors. This is due to an

*david.niepce@chalmers.se

enhanced participation ratio [17] of the TLS host volume, within dielectrics, to the total volume threaded by the electric field.

In this paper, we demonstrate a nanowire-based superinductor with a characteristic impedance of 6.795 kΩ. We developed a process, based on dry etching of a hydrogen silsesquioxane (HSQ) mask defined by high-resolution electron-beam lithography, to pattern a 20-nm-thick film of niobium nitride (NbN) into a 40-nm wide and approximately 680-μm-long nanowire. This is sufficiently narrow to ensure a large inductance and sufficiently wide to exponentially suppress unwanted phase slips of the superconducting order parameter [21]. The thickness is chosen so as to yield a strongly but not excessively disordered film to balance the requirements of high kinetic inductance and low losses. We study both the microwave transmission and dc transport properties of several nanowires to characterize their impedance and microwave losses: they exhibit a quality factor at single-photon excitation of 2.5×10^4, which is comparable to JJA-based superinductors [6]. We find that the dominant loss mechanism is parasitic TLS, which is exacerbated by the unfavorable TLS participation ratio [17] that arises from the small dimensions required to obtain a high impedance.

II. METHODS

The measured sample contains five nanowires that are inductively coupled to a common microwave transmission line. It also contains separate dc transport test structures. Figures 1(a) and 1(b) show micrographs of a typical device. The fabrication process is detailed in Appendix A and materials and design considerations in Appendix D.

We study the microwave properties of these resonators by measuring the forward transmission (S_{21}) response. In a similar way to the devices measured in Ref. [13], the coupling to the fundamental mode in our resonators is extremely weak. Therefore, in the following, we focus our study on the next resonant mode. Figure 1(c) shows a typical S_{21} magnitude response measured at 10 mK and with an average photon population $\langle n \rangle = 1$. We determine the resonator parameters by fitting the data with an open-source traceable fit routine [27], from which we find a resonant frequency $f_r = 4.835$ GHz and an internal quality factor $Q_i = 2.5 \times 10^4$. Detailed experimental methods are included in Appendices B–C.

III. RESULTS AND DISCUSSION

To understand this resonance, we first study the transport properties of our NbN nanowires. We estimate the kinetic inductance contribution $L_k^{\square}(0)$ using [28]

$$L_k^{\square}(0) = \frac{\hbar R_N^{\square}}{\pi \Delta_0}, \qquad (1)$$

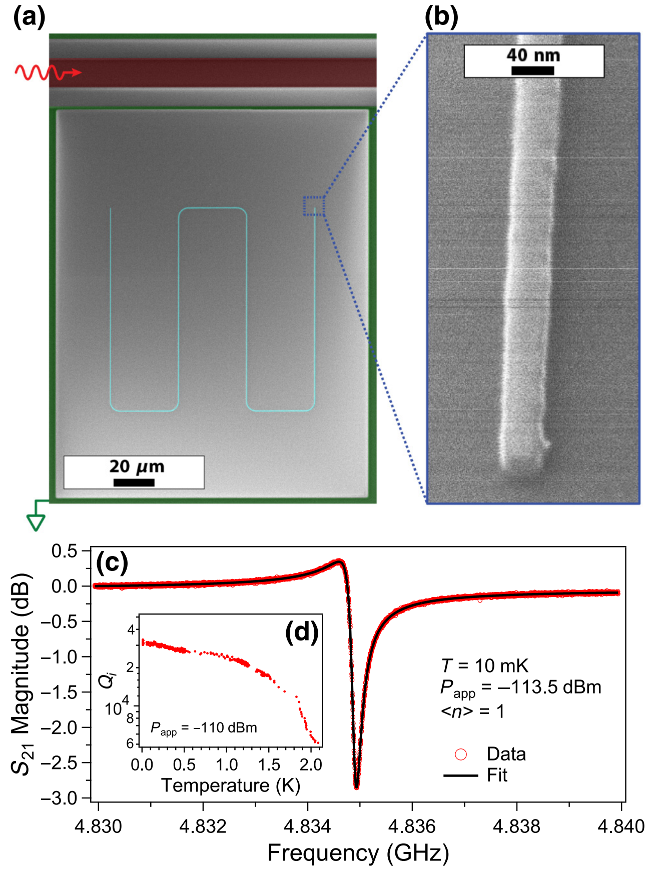

FIG. 1. (a) False-color scanning electron microscope micrograph of a nanowire resonator coupled to a microwave feed line; the NbN feed line is shown in red, the NbN ground planes are shown in green, the exposed Si substrate where NbN has been etched away is in gray and the 40 nm × 680 μm nanowire is highlighted in cyan. (b) A helium focused ion beam image of the nanowire highlighting a very good line edge roughness and a low concentration of shape defects. (c) S_{21} magnitude response of the device, in the single-photon regime. The black line is a fit to determine the resonance parameters. (d) A plot of the internal quality factor Q_i of a nanowire superinductor resonator as a function of temperature.

where $R_N^{\square}$ is the normal-state sheet resistance, $\hbar$ the reduced Planck constant, and Δ_0 the superconducting gap at zero temperature. NbN is experimentally found to be a strongly coupled superconductor with $\Delta_0 = 2.08 k_B T_c$ [2], where T_c is the critical temperature and k_B is the Boltzmann constant. By measuring the $R(T)$ characteristic we find $R_N^{\square} = 503\ \Omega/\square$ and $T_c = 7.20$ K. Using Eq. (1), this yields $L_k^{\square}(0) = 82$ pH/□. For a 40-nm-wide nanowire, this corresponds to an inductance per unit length of 2.05 mH m^{-1}. From an empirical formula [29], the magnetic inductance, due to the geometry of the nanowire, is estimated to be only $L_m \simeq 1\ \mu$H m^{-1}. Therefore, we assume that the nanowire inductance arises entirely from the kinetic inductance, so that $L_{NW} = L_k$. Further materials and geometrical

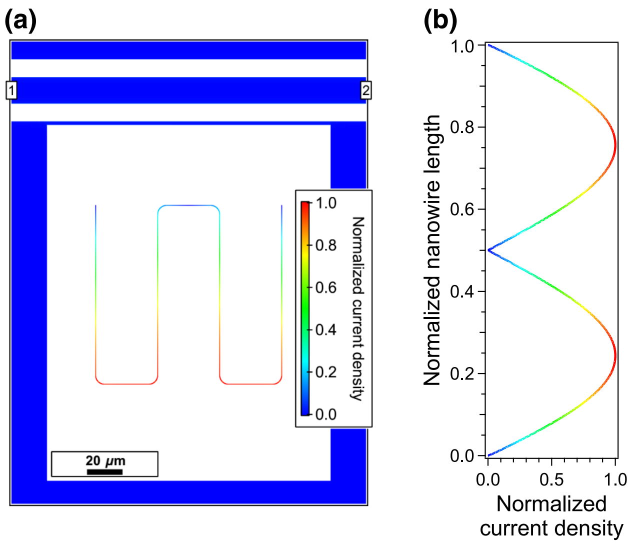

FIG. 2. (a) Microwave simulation of the current density in the device for the second resonant mode. (b) Normalized current density along the nanowire extracted from the simulation. The obtained mode structure is consistent with the second mode of a distributed $\lambda/2$ resonator. See also Appendix D 2 c and Figs. 10–11.

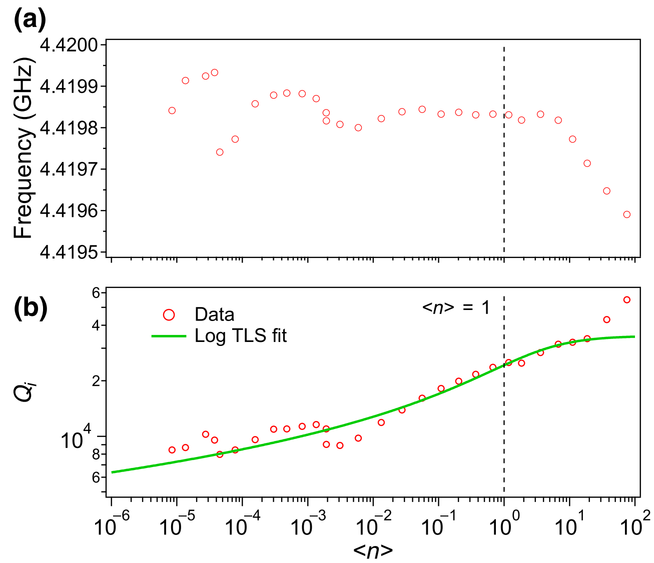

FIG. 3. (a) Resonant frequency of a typical nanowire resonator as a function of microwave drive. (b) Internal quality factor (Q_i) of a typical nanowire superinductor resonator as a function of the microwave drive. The solid line is a fit to Eq. (3). The vertical dashed lines highlight the single microwave photon regime.

considerations for nanowires are explained in detail in Appendix D.

We simulate our devices using Sonnet *em* microwave simulator. The simulation results, shown in Figs. 2(a) and 2(b), confirm that our device behaves as a distributed $\lambda/2$ resonator with a well-defined wave impedance (see also Appendix D 2 c). From the simulation we also estimate the capacitance per unit length to be $C_{\mathrm{NW}} = 44.4\ \mathrm{pF\,m^{-1}}$. Combining these properties leads to estimated resonant frequencies within 1% of the measured f_r for all of our resonators. Using these parameters, we calculate the characteristic impedance of our nanowires to be $Z_c = \sqrt{L_{\mathrm{NW}}/C_{\mathrm{NW}}} = 6.795\ \mathrm{k\Omega} \pm 35\ \Omega$. Therefore, $Z_c \geq R_Q$, indicating that they are indeed superinductors.

Having demonstrated superinductors, we now examine their behavior as a function of applied microwave drive and varying temperature. We first determine the range of temperatures at which we can operate our device. Figure 1(d) shows a measurement of the internal quality factor Q_i against temperature. We show that from 10 mK to 1.4 K, it only marginally decreases from 3×10^4 to 2×10^4. This offers a far greater range of operation than aluminum JJA-based superinductors, which show significant dissipation above 100 mK [6].

We now investigate the low-temperature loss mechanisms as a function of microwave power. When probed with an applied power P_{in}, the average energy stored in a resonator of characteristic impedance Z_c is given by $\langle E_{\mathrm{int}}\rangle = \langle n\rangle/hf_r = Z_0 Q_l^2 P_{\mathrm{in}}/\pi^2 Z_c Q_c f_r$, where $\langle n\rangle$ is the average number of photons in the resonator, h is Planck's constant, $Z_0 = 50\ \Omega$, and Q_c and Q_l are the coupling and loaded quality factors, respectively. Due to the large characteristic impedance of our resonator, we are able to measure in the low photon regime with a high applied power. Consequently, this enables us to measure, with good signal-to-noise ratio (without using a quantum-limited parametric amplifier), photon populations 2 to 3 orders of magnitude lower than in conventional resonators.

In Fig. 3(a), starting at $\langle n\rangle = 1$, as we increase the power, the resonant frequency does not change until $\langle n\rangle \simeq 10$. Upon a further increase of the power, the frequency decreases until the resonator bifurcates. This is explained by the power dependence of the kinetic inductance, which behaves as a Duffing-like nonlinearity [30]. We note that this nonlinearity occurs at similar microwave drive powers as for junction-embedded resonators [31]. Starting again at $\langle n\rangle = 1$, as we now decrease the power, we see the frequency remains approximately constant. As $\langle n\rangle$ is decreased below $\langle n\rangle \simeq 10^{-3}$, the resonator exhibits frequency jitter consistent with TLS-induced changes of the permittivity $\epsilon(f)$ [32]. This frequency noise results in spectral broadening of the resonance curve.

We now examine the internal quality factor as a function of applied microwave power. In Fig. 3(b), within the power range between $\langle n\rangle \simeq 10^{-5}$ and $\langle n\rangle \simeq 10^{-3}$, we find that Q_i is approximately constant, with changes in the fitted value caused by frequency-jitter-induced spectral broadening. As we increase the power from $\langle n\rangle \simeq 10^{-3}$, Q_i increases, which is consistent with depolarization of TLS. For $\langle n\rangle \geq 40$, Q_i is overestimated due to the Duffing nonlinearity.

In order to fit the data, it is usual to sum inverse quality factors to produce a loss model that can distinguish different loss channels. Of these quality factors, we first consider the dielectric loss of a capacitor, which is described by $1/Q_{\text{cap}} = \epsilon''/\epsilon'$. Conventionally, we label this in terms of TLS susceptibility $[\chi(f) = \epsilon(f) - 1]$, which can be split into a real (dispersive) term $\chi'(f)$, and an imaginary (dissipative) term $\chi''(f)$ [33,34]. Typically, data such as that in Fig. 3(b) is fitted to a loss model based on $\chi''(f)$ [26,35], where the resulting quality factor is justified either by simulation [36] or by measurement of a tanh-like temperature dependence [26]. However, unless the statistics of Q_i are sufficient to reliably extract the mean [37], this approach can suffer from errors in determining the TLS quality factor. This spread in Q_i arises from spectral instability of TLS [32,38,39], which leads to a time-varying number of near-resonant TLS. Crucially, $\chi''(f)$ is strongly peaked [33] (Lorentzian-like) and therefore is particularly sensitive to fluctuations of a narrow spectrum of TLS.

Instead, it is preferable to determine the TLS losses by using $\chi'(f)$, which can be accurately inferred from a measurement of the shift of the resonant frequency as a function of temperature, $\Delta f(T)$. The real part χ' decays slowly in frequency [33], in contrast to χ'', and therefore is robust against spectral instabilities. Consequently, $\chi''(f)$ can be determined from $\chi'(f)$ by the Kramers-Kronig relation to reliably determine the TLS-related quality factor, whose inverse is then called the *intrinsic* loss tangent, $F\delta^i_{\text{TLS}}$ [17].

To measure $\Delta f(T)$ we lock onto the resonant frequency using a Pound frequency-locked loop (PFLL) [32,40], and continuously track frequency changes of the resonator as we vary the temperature (See Appendix C for details of the experimental setup). TLS can become thermally excited and the multiple TLS states correspond to different permittivity (susceptibility, i.e., capacitance): as we vary the temperature, the permittivity changes and therefore the frequency changes. Figure 4(a) shows the changes in resonant frequency against the natural energy scale of the TLS (hf_r/k_BT) for temperatures ranging from 10 mK to 1 K. This frequency shift is described by [17]

$$\Delta f(T) = F\delta^i_{\text{TLS}} \left\{ \ln\left(\frac{T}{T_0}\right) - [g(T,f_r) - g(T_0,f_r)] \right\}, \quad (2)$$

where $\Delta f(T) = [f_r(T) - f_r(T_0)]/f_r(T_0)$, T_0 is a reference temperature, the participation ratio F is the ratio of electric field threading TLS to the total electric field, $g(T,f) = \text{Re}\left[\Psi\left(\frac{1}{2} + hf/2\pi i k_B T\right)\right]$, and Ψ is the complex digamma function.

We use Eq. (2) to fit the measured data in Fig. 4. Importantly, this expression only fits the TLS contribution but does not fit the temperature-dependent kinetic-inductance contribution, which occurs below $hf_r/k_BT = 0.1$. Table I contains the resulting values for the intrinsic loss tangent $F\delta^i_{\text{TLS}}$, which, in turn, can be used to fit the data in Fig. 3 using a model that takes TLS interactions into account [32,41]:

$$\frac{1}{Q_i} = F\delta^i_{\text{TLS}} P_\gamma \ln\left(\frac{cn_c}{\langle n\rangle} + \delta'_0\right) \tanh\left(\frac{hf_r}{2k_BT}\right). \quad (3)$$

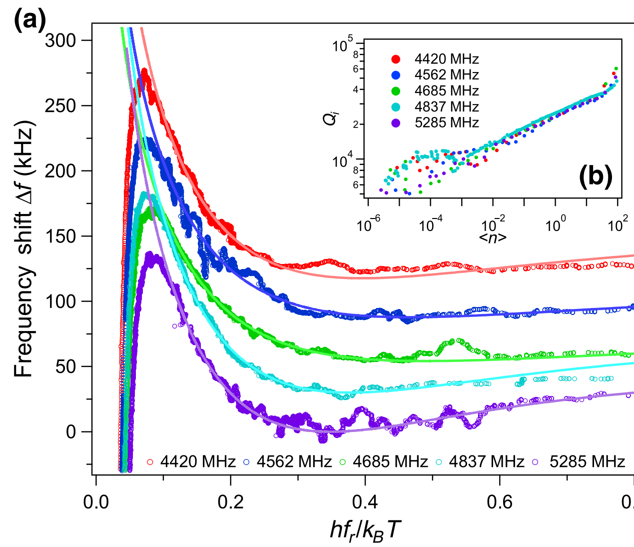

FIG. 4. (a) Frequency shift Δf as a function of the normalized frequency f_r of all measured nanowire superinductor resonators. The data is experimentally obtained with the PFLL by tracking the changes in resonant frequency against temperature between 10 mK and 1 K. The solid lines show fits to the theory described by Eq. (2). For clarity, the curves have been offset by 30 kHz. (b) Q_i vs microwave drive power for the same nanowire superinductor resonators (cf. Fig. 3).

Here c is a large constant, δ'_0 is the log-scaled next dominant loss rate and P_γ is the TLS switching rate ratio, defined by $P_\gamma = 1/\ln(\gamma_{\max}/\gamma_{\min})$ where $\gamma_{\max}$ and $\gamma_{\min}$ are the maximum and minimum rate of TLS switching, respectively. These rates have been measured in the TLS-related charge-noise spectrum of single-electron transistors. They were found to extend from $\gamma_{\min} \simeq 100$ Hz to $\gamma_{\max} \simeq 25$ kHz [42], corresponding to $P_\gamma = 0.18$. Our fitted values of P_γ are summarized in Table I: we find values between 0.153 and 0.218, in good agreement with this estimate and other results [40,43,44]. Table I also details the next dominant (i.e., non-TLS) loss term, δ'_0; this number represents an upper bound (of the loss, or equivalently, lower bound of the Q'_0) due to the onset of bifurcation. Examination of any temperature dependence of δ'_0 could be used to pin down whether the residual loss arises due to quasiparticles or other mechanisms.

We have demonstrated that dissipation in our nanowires is not an intrinsic property of disorder within the film [24,25] but is instead caused by TLS. This is not surprising as TLS are the predominant source of dissipation

TABLE I. Nanowire superinductance resonator parameters. $F\delta^i_{\mathrm{TLS}}$ is obtained from fits to Eq. (2), P_γ and δ'_0 from fits to Eq. (3).

NW $f_r(Mhz)$	$F\delta^i_{\mathrm{TLS}}$ $(\times 10^{-5})$	P_γ	δ'_0
4420	4.37	0.195	≤ 28.3
4562	3.84	0.183	≤ 47.5
4685	3.53	0.218	≤ 41.8
4837	4.40	0.153	≤ 48.4
5285	4.12	0.213	≤ 28.1

and decoherence in a wide variety of quantum devices. An important consideration is the role of the TLS participation ratio. The ratio of E field threading TLS to the total E field is known to scale as approximately $1/\bar{w}$ [17], where $\bar{w}$ is the center conductor width of a resonator. Consequently, the 40-nm width used here to produce a superinductor leads to an unfavorable participation ratio and therefore a much lower Q_i than is found for wider, micrometer-sized resonator geometries. Additionally, the nanowire lithography relies on the use of a spin-on glass resist (HSQ), which resembles amorphous silicon oxide. Silicon oxide is a well-known host of TLS [45] and because some HSQ remains unetched atop our nanowires, we suspect that this is the dominant source of TLS in our devices. Therefore, improvements to the fabrication, specifically the nontrivial removal of the HSQ mask should result in significant improvements in device performance.

IV. CONCLUSION

In conclusion, we demonstrate a nanowire superinductance with a characteristic impedance of 6.795 kΩ and a quality factor at single-photon excitation of $Q_i = 2.5 \times 10^4$. This quality factor is comparable to both JJA-based superinductors [6] and the temperature-scaled TLS loss $[\tanh(hf_r/2k_BT)]$ in similar nanowire resonators [13]. We have analyzed the loss mechanisms in our devices and find TLS to be the dominant cause of loss, which is in contrast to the high rates of dissipation found in other nanowire [4,21] or strongly disordered thin film devices [24]. We emphasize that demonstrating that nanowires losses are "conventional" is a important step forward for all nanowire-based quantum circuits. Therefore, this enables long-lived nanowire-based superconducting circuits, such as a nanowire fluxonium qubits [10], improved phase-slip qubits [4,21], or other circuits benefiting from high-inductance, high-impedance devices.

ACKNOWLEDGMENTS

The authors thank O.W. Kennedy for He FIB imaging of our devices. We acknowledge useful discussions with S.E. Kubatkin, A.V. Danilov, and P. Delsing as well as support from the Chalmers Nanofabrication Laboratory staff. This research has been supported by funding from the Swedish Research Council and Chalmers Area of Advance Nanotechnology.

APPENDIX A: SAMPLE FABRICATION

Samples are fabricated on high-resistivity ($\rho \geq 10$ kΩ cm) (100) intrinsic silicon substrates. Before processing, the substrate is dipped for 30 s in hydrofluoric acid (HF) to remove any surface oxide. Within 5 min, the wafer is loaded into a UHV sputtering chamber where a 20-nm-thick NbN thin film is deposited by reactive dc magnetron sputtering from a 99.99% pure Nb target in a 6:1 Ar:N_2 atmosphere. A 500-nm-thick layer of PMMA A6 resist is spin coated and then exposed with electron-beam lithography (EBL) to define the microwave circuitry. After development, the pattern is transferred to the film by reactive ion etching (RIE) in a 50:4 Ar:Cl_2 plasma at 50 W and 10 mTorr. The nanowires are patterned in a subsequent EBL exposure using a 50-nm layer of hydrogen silsesquioxane (HSQ), an ultra-high-resolution negative resist suitable for ≤ 10 nm features [46].

A common problem with HSQ is the formation of small agglomerates that are not completely dissolved during development. These small particles tend to accumulate on the edges of developed structures and act as micromasks when the pattern is etched. From FIB micrographs of our devices (see Fig. 5), we estimate a lithographic defect rate of less than three defects per 10 μm and that each defect contributes to the geometry of the device as approximately one square. For a 680-μm long and 40-nm nanowire, this translates to a maximum uncertainty in the total number of squares of $n_\square = 17\,000 \pm 200$ squares, which is consistent with the 1% error reported in the main text.

APPENDIX B: TRANSPORT CHARACTERIZATION

As described in the main text, we estimate the kinetic inductance contribution $L^\square_k(0)$ in our devices using [28]

$$L^\square_k(0) = \frac{\hbar R^\square_N}{\pi \Delta_0}. \tag{B1}$$

For that purpose, we measure the $R(T)$ characteristic of our nanowires as shown in Fig. 6. We observe that from room temperature, as the temperature decreases, the resistance increases until a plateau is reached at about 15 K. This behavior is typical of weak localization in strongly disordered materials [47]. As the temperature further decreases from 15 K, the resistance starts to decrease and we observe a 2-K-wide superconducting transition.

The width of this superconducting transition can be fully described by two different mechanisms. Above T_c, thermodynamic fluctuations give rise to short-lived Cooper pairs,

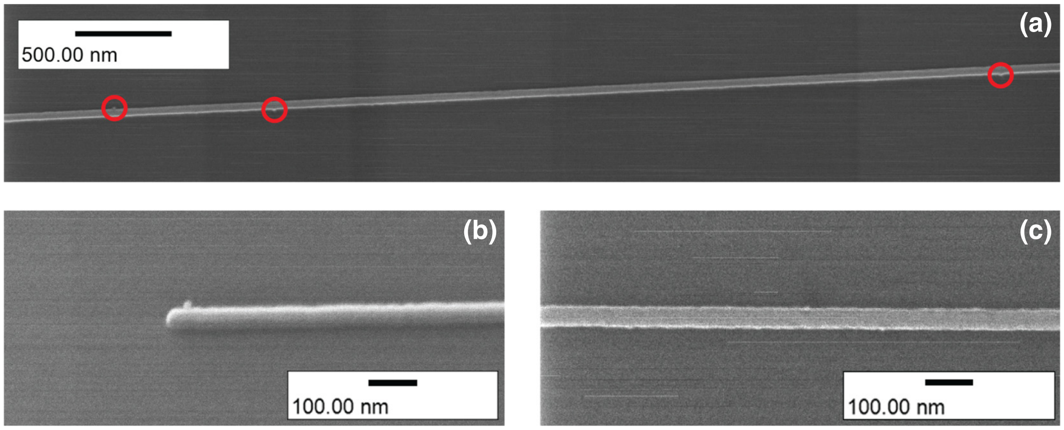

FIG. 5. Helium FIB micrographs of a nanowire superinductor, courtesy of O.W. Kennedy, University College London. (a) Low-magnification image of a long section (5.5 μm) of the nanowire. Lithographic defects are circled in red. (b) High-magnification image of the end of the nanowire. Here we can see that the defect is approximately 10-nm wide. (c) High-magnification image of a section of nanowire without defects. Here we see that the edge roughness is approximately ± 1 nm.

which increase the conductivity. These conductivity fluctuations have been described in the 2D case by Aslamasov and Larkin [28] and are given by

$$\sigma_{2\mathrm{D}}(T) = \frac{e^2}{16\hbar d}\left(\frac{T_c}{T - T_c}\right), \tag{B2}$$

where T is the temperature, e is the electron charge, and d is the film thickness. The total conductivity above T_c is now expressed as $\sigma(T) = \sigma_n + \sigma_{2\mathrm{D}}(T)$.

Below T_c, the resistance does not immediately vanish. This can be explained by a Berezinskii-Kosterlitz-Thouless (BKT) transition [48] where thermal fluctuations excite pairs of vortices. These vortex-antivortex pairs (VAP) are bound states, formed by vortices with supercurrents circulating in opposite directions. Above the ordering temperature T_{BKT}, VAPs start to dissociate and their movement cause the observed finite resistance. This resistivity is described by [48]

$$\rho(T) = a \exp\left(-2\sqrt{b\frac{T_c - T}{T - T_{\mathrm{BKT}}}}\right), \tag{B3}$$

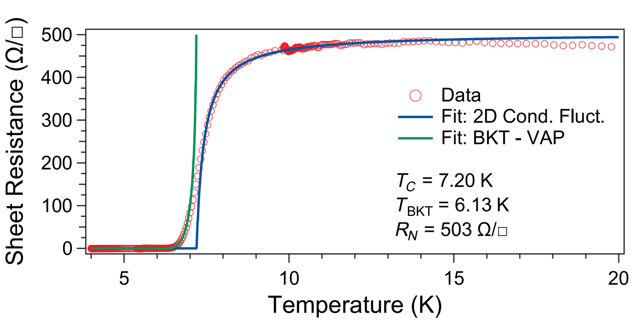

FIG. 6. $R(T)$ characteristic of an NbN nanowire. The blue and green lines are fits to Eqs. (B2) and (B3), respectively.

with $T_{\mathrm{BKT}} < T < T_c$, and where a, b are material-dependent parameters.

By fitting the $R(T)$ to Eqs. (B2)–(B3), $R_N^{\square}$ and T_c can be obtained and $L_k^{\square}(0)$ is then calculated using Eq. (1).

APPENDIX C: MEASUREMENT SETUP

The sample is wire bonded in a connectorized copper sample box that is mounted onto the mixing chamber stage of a Bluefors LD250 dilution refrigerator [Fig. 7(a)]. The inbound microwave signal is attenuated at each temperature stage by a total of 60 dB before reaching the device under test. Accounting for cable losses and sample-box insertion loss, the total attenuation of the signal reaching the sample is 70 dB. To avoid any parasitic reflections and noise leakage from amplifiers, the transmitted signal is fed through two microwave circulators (Raditek RADI-4.0-8.0-Cryo-4-77K-1WR) and a 4–8-GHz band-pass filter. Finally, the signal is amplified by a LNF LNC4_8A HEMT cryogenic amplifier (45-dB gain) installed on the 2.8-K stage. Additional amplification is done at room temperature (Pasternack PE-1522 gain-block amplifiers).

This microwave setup is connected to a vector network analyzer (Keysight PNA-X N5249A or R&S ZNB20) for initial characterization and quality-factor measurements of the nanowire resonators at various excitation powers [Fig. 7(a)]. However, as highlighted in the main text, at low drive powers, VNA measurements require significant amounts of averaging to increase the SNR. At low microwave energies, frequency jitter leads to spectral broadening.

To reliably determine the TLS loss contribution, we instead measure the resonant frequency of the resonator against temperature [17,49]. For that purpose, the microwave setup is included in a frequency-locked loop

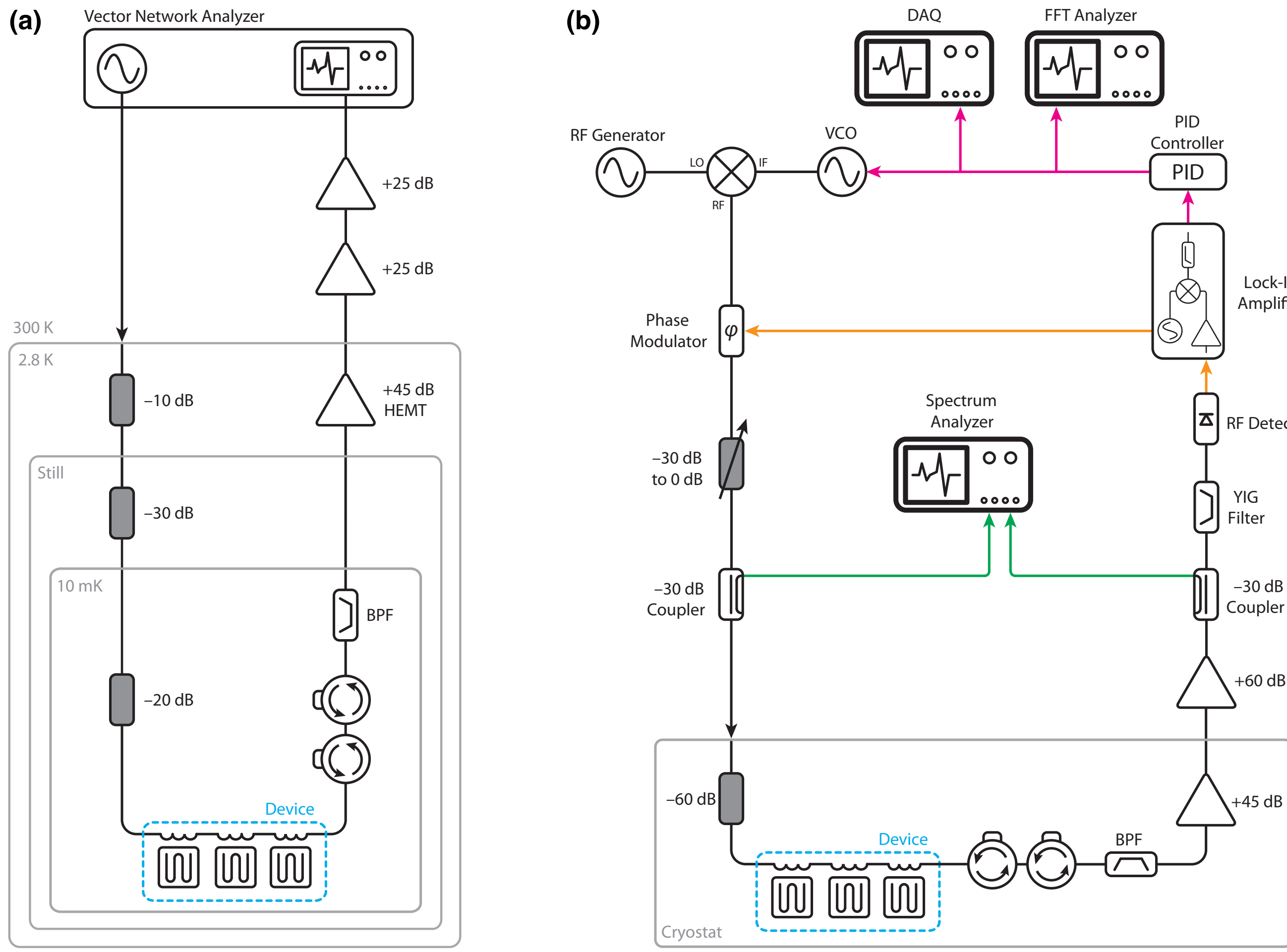

FIG. 7. (a) Cryogenic microwave setup. (b) Schematic of the Pound frequency-locked loop (PFLL).

using the so-called Pound locking technique [Fig. 7(b)]. Originally developed for microwave oscillators [50], this technique is commonly used in optics for frequency stabilization of lasers [51] and has been recently used for noise [49,52] and ESR [40,53] measurements with superconducting microwave resonators. In this method, a carrier signal is generated by mixing the output of a microwave source (Keysight E8257D) and a VCO (Keysight 33622A) operating at 50 MHz. This carrier is phase-modulated (Analog Devices HMC538) before being passed through the resonator under test. The phase modulation frequency is set so that the sidebands are not interacting with the resonator and therefore only the central tone undergoes a phase shift while the sidebands pass unaltered. After amplification, the signal is filtered (MicroLambda MLBFP-64008) to remove the unwanted mixer image and rectified using an rf detector diode (Pasternack PE8016). The diode output is demodulated with a lock-in amplifier (Zurich Instruments HF2LI). The principle of operation is close to that of the PLL; however, the phase modulation allows for a common-mode rejection of any phase fluctuations. An additional benefit is that the readout is done at a higher frequency (2 MHz vs dc), which reduces any parasitic electronic noise.

The feedback loop consist of an analog PID controller (SRS SIM960) locked on the zero crossing of the error signal. This gives an output directly proportional to any shift in resonant frequency of the resonator. This output signal is then used to drive the frequency modulation of the VCO, varying its frequency accordingly and enabling the loop to be locked on the resonator.

In this work, we only sample the PID output slowly ($\leq$ 100 Hz) to track frequency changes (Keithley 2000), but noise in the resonator can also be studied using a frequency counter (Keysight 53132A), a fast-sampling DAQ (NI PXI-6259 DAQ) or an FFT analyzer (Keysight 35670A). This will be the focus of future work.

APPENDIX D: PRACTICAL CONSIDERATIONS FOR NANOWIRE SUPERINDUCTORS

As described in the main text, a superinductor is a low-loss circuit element with characteristic impedance Z_c larger than the superconducting resistance quantum R_Q. This is a natural definition as charge and flux are electromagnetic dual quantities, whose competing quantum fluctuations become equal in strength at $Z = R_Q$, at which point the magnitudes of the respective zero-point quantum fluctuations (rms) are half a Cooper pair and half a flux quantum, respectively [54].

These prerequisites pose several constraints on the successful design of a superinductor: in the context of disordered superconductors, this implies that the thin film should have a high kinetic inductance while the fabricated structure should have a capacitance as low as possible. In this appendix, we detail the implications of these constraints on several aspects of the design of a nanowire superinductor.

1. Materials

In the main text and in Appendix B, we highlight that the kinetic inductance contribution for a disordered superconductor is derived using the Mattis-Bardeen framework (Eq. 1). This formula reveals that in order to achieve a highly inductive film, we need a superconductor that exhibits a high normal-state resistance R_N and a small superconducting gap (i.e., a small critical temperature T_c).

However, there are several caveats in this simple interpretation. First of all, while a small gap is favorable for a high inductance, a working temperature too close to T_c leads to the presence of quasiparticles. In turn, these quasiparticles lead to significant losses and breach the low-loss criterion for a superinductor. This therefore imposes a practical limit on the critical temperature of the superconductor to realize such a device: for a practically obtainable temperature of 10 mK, the minimum practical critical temperature is around 1 K.

Additionally, while it is tempting to arbitrarily increase R_N (i.e., the level of disorder) to achieve a high kinetic inductance, films exhibit disorder-related losses as they get close to the superconductor-insulator transition [20–24]. A recent theory attributes these losses to the presence of low-lying subgap states in the proximity of the superconducting-insulating transition [25]. Experimentally, disorder-induced subgap states [2] and spatial inhomogeneity of the gap [3] were demonstrated for NbN thicknesses below about 6 nm. Consequently, we need to fabricate a sufficiently disordered (thin) superconductor to obtain high inductance, but not so disordered as to induce dissipation.

In this work, our choice of superconductor is niobium nitride. NbN has a high bulk critical temperature (16 K), however, the critical temperature is suppressed as the thickness of the film is reduced [55], which leads to a favorable scaling of the superconducting gap in Eq. (1). After a careful optimization of the NbN thin-film fabrication, a target thickness of 20 nm, corresponding to a critical temperature $T_c = 7.20$ K, and a normal-state resistance $R_N = 503\ \Omega/\square$ represent a good compromise between disorder and kinetic inductance, with a corresponding sheet kinetic inductance $L_k = 82$ pH/$\square$.

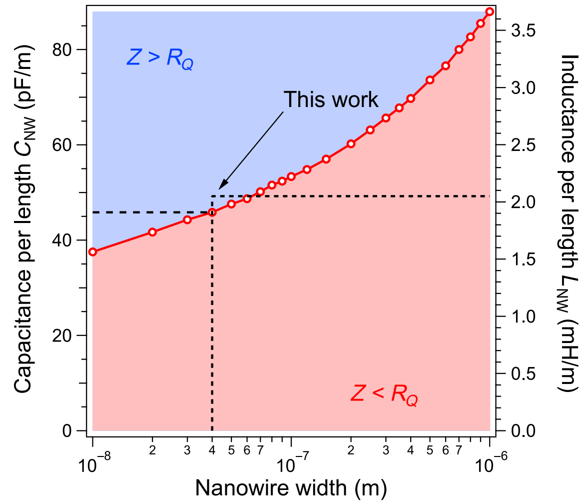

FIG. 8. Simulated capacitance per unit length, $C_{\mathrm{NW}}(\bar{w})$ (red circles), for nanowire widths $\bar{w}$ ranging from 1 μm down to 10 nm. The right axis corresponds to the minimum inductance per unit length, $L_{\mathrm{NW}}(\bar{w})$, required to obtain a characteristic impedance $Z_c = [L_{\mathrm{NW}}(\bar{w})/C_{\mathrm{NW}}(\bar{w})]^{1/2} > R_Q$. The superinductance regime – the area highlighted in blue – should be understood as the range in which $L_{\mathrm{NW}}(\bar{w})$ is sufficiently high, for a fixed $\bar{w}$, that it will yield $Z > R_Q$.

2. Geometry

a. Nanowire geometry

In the previous section, we establish that because of losses we cannot arbitrarily increase the inductance to maximize the impedance. Therefore, to realize a superinductor, it becomes crucial to minimize the stray capacitance, which can be achieved with a nanowire geometry. We simulate the capacitance per length for several nanowires with widths varying from 1 μm down to 10 nm. The results are shown in Fig. 8. This figure also shows the corresponding minimum inductance per length required for a superinductance.

b. TLS filling factor (participation ratio)

In the main text, we highlight the role of the TLS filling factor in the losses and mention that reducing the physical dimensions of a resonator leads to an unfavorable scaling. To support this claim, we simulate the TLS filling factor using an electrostatic simulation in COMSOL for nanowires of various width. In our model, we assume a TLS host volume V_{TLS} consisting of a 10-nm-thick layer of silicon oxide and a 30-nm-thick layer of HSQ (modeled as silicon oxide). The filling factor is obtained by calculating the ratio of the electric energy stored in the TLS host volume

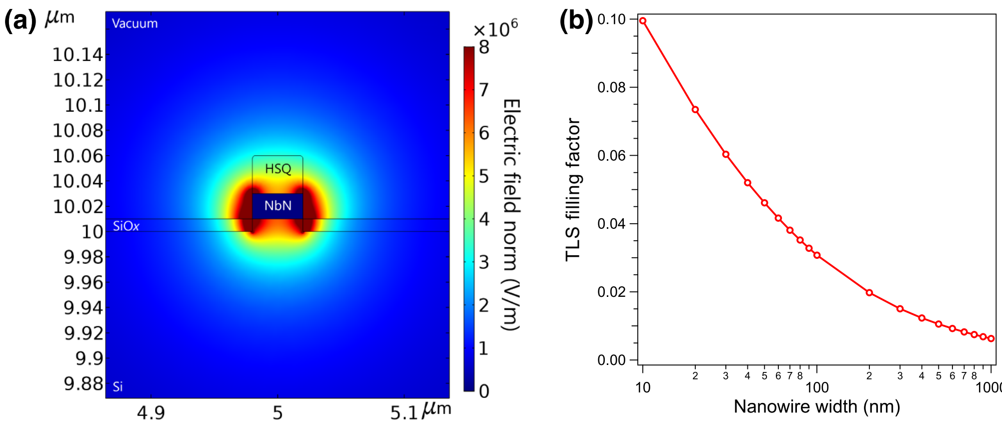

FIG. 9. (a) Magnitude of the electric field for a 40-nm-wide nanowire. (b) TLS filling factor for nanowire widths ranging from 1 μm down to 10 nm.

to the total electric energy [56]:

$$F = \frac{\int_{V_{\mathrm{TLS}}} \varepsilon_{\mathrm{TLS}} \vec{E}^2 d\vec{r}}{\int_V \varepsilon \vec{E}^2 d\vec{r}}. \tag{D1}$$

The results of the simulation are shown in Fig. 9. We note the significant increase of the filling factor as the width is reduced.

c. Parasitic capacitance of meanders

In this section, we analyze the geometry-dependent parasitic capacitance due to meandering of the nanowire. For that purpose, we simulate the frequency response and current density using Sonnet *em* microwave simulator. In order to reduce meshing and simulation times, we simulate 100-nm-wide wires in a simple step-impedance resonator geometry. We start by simulating a straight wire as a reference and then proceed to a meandered geometry with a fixed meander length $b = 20\,\mu$m while gradually decreasing the distance between meanders from $a =$ 30 μm (typical distance in our devices) to 100 nm (see Fig. 10).

Figures 10 and 11 show the normalized current density along the nanowires at the fundamental resonant frequency of the simulated structure. To be clear, for meandered geometries, the current density is not measured as a line cut along the x axis, but instead the geometry is unwound and the current density is extracted at every point along the nanowire. We observe that for the straight wire and for meanders with $a > 5\ \mu$m, the current density is consistent with the expected $\lambda/2$ mode structure of such a resonator and the characteristic impedance is well defined to $Z_c = \sqrt{L_{\mathrm{NW}}/C_{\mathrm{NW}}}$ as described in the main text.

However, below $a = 5\ \mu$m, we observe that, as the distance between the meanders is reduced, the resonant frequency significantly diverges from the straight nanowire reference value and the current density is severely distorted [57]. This is explained by the increasing influence of parasitic capacitance between each meander. This parasitic capacitance is equivalent to shunting the nanowire with an extra capacitance and lowering its characteristic

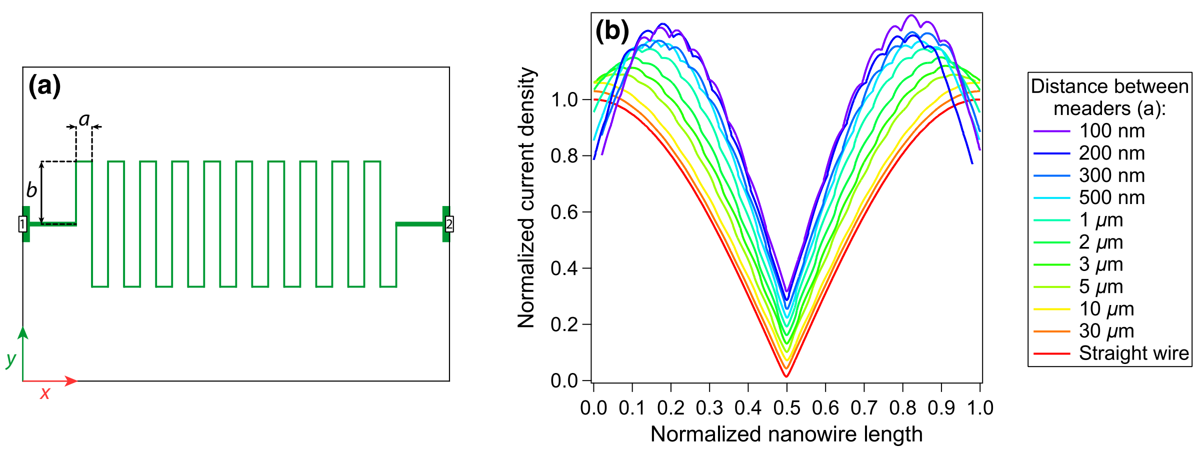

FIG. 10. (a) Schematic representation of a typical meandered nanowire resonator structure simulated in this section. a and b are the distance between meanders and the meander length, respectively. 1 and 2 are the excitation and measurement ports and the black outline represents the grounded edge of the simulation box. (b) Normalized current densities at the fundamental resonance frequencies for all the simulated structures. For clarity, the curves have been offset by 0.03.

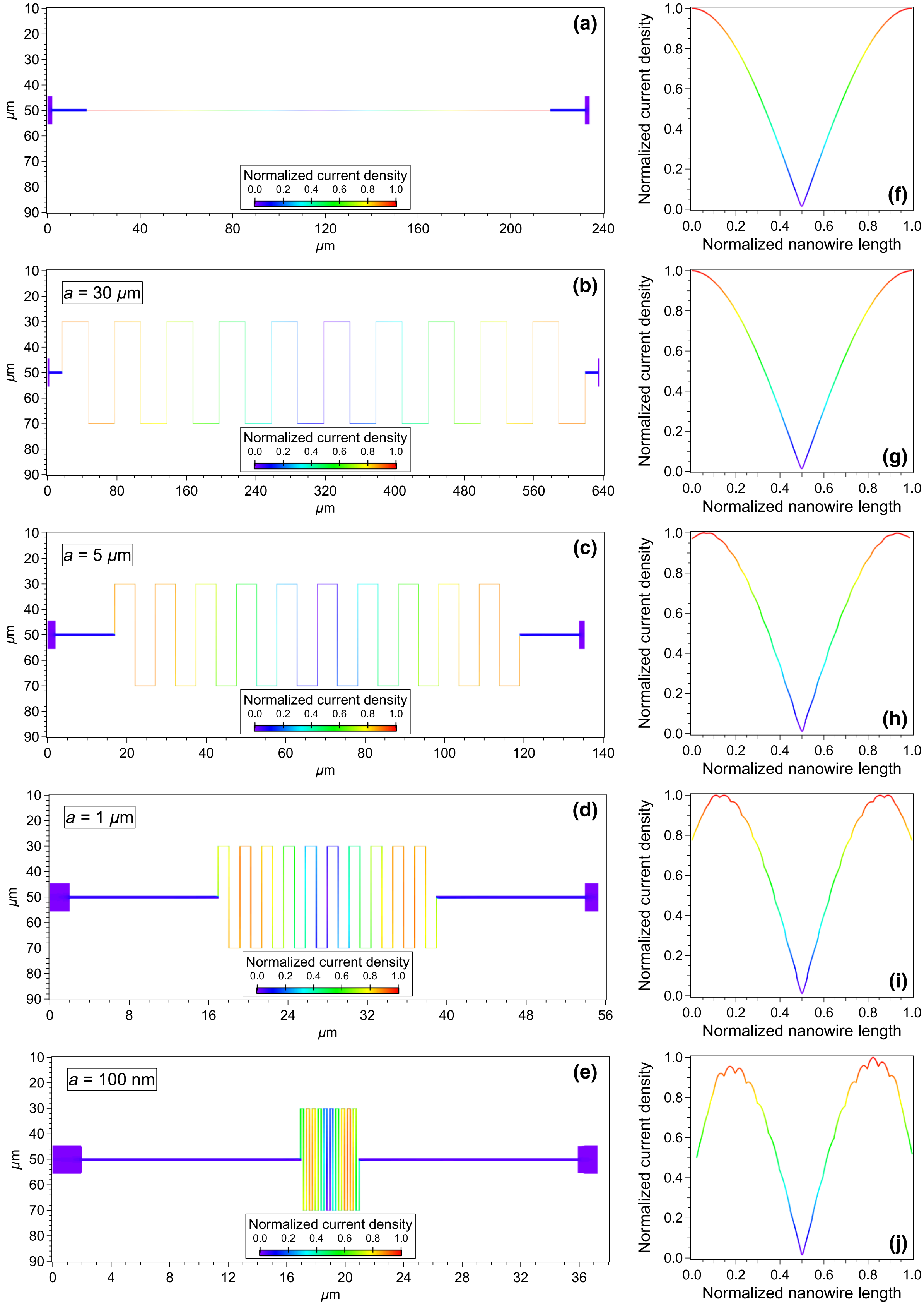

FIG. 11. (a)–(e) Current density distribution in nanowires at several inter-meander distances. (f-j) Corresponding normalized current density along the nanowire.

TABLE II. Nanowire superinductance film and device parameters.

Parameter	Symbol	Value
Normal-state sheet resistance	$R_N^{\square}$	503 $\Omega\square$
Sheet kinetic inductance	$L_k^{\square}$	82 $pH/\square$
Nanowire length	l	680 μm
Nanowire width	$\bar{w}$	40 nm

impedance. Moreover, the structure then cannot be treated as a $\lambda/2$ resonator anymore and therefore has no well-defined wave impedance.

d. Exponentially suppressed phase-slip rate

In the main text, we make the argument that the device dimensions are chosen to exponentially suppress phase slips. We estimate the phase-slip rate $\Gamma_S = E_S/h = E_0/h\exp(-\kappa\bar{w})$ for our device within the phenomenological model for strongly disordered superconductors. Our analysis is similar to that of Peltonen *et al.* [21]. In this model, E_S is the phase-slip energy and we have $E_0 = \rho\sqrt{l/\bar{w}}$, where l and $\bar{w}$ are the nanowire length and average width, respectively, $\rho = (\hbar/2e)^2/L_k^{\square}$ represents the superfluid stiffness, $\kappa = \eta\sqrt{\nu_p\rho}$, $\eta \simeq 1$, and $\nu_p = 1/(2e^2R_N^{\square}D)$ is the Cooper-pair density of states with $D \simeq 0.45\,\mathrm{cm}^2\,\mathrm{s}$. For our device parameters (summarized in Table II), we find $\Gamma_S \simeq 7\times10^{-5}$ Hz. This corresponds to an average of one phase-slip event every 4 h, which is entirely negligible.

APPENDIX E: CONVENTIONAL AND INTERACTING (LOG) TLS MODELS

Traditionally, the loss of superconducting microwave devices is parameterized by a model, which splits the loss into a power-dependent term, associated with TLS, and a power-independent term (δ_0), associated with resistive losses (quasiparticles) or parasitic microwave modes. An example of this model is described by [26]

$$\frac{1}{Q_i} = \delta^i_{\mathrm{tot}} = F\delta^0_{\mathrm{TLS}}\frac{\tanh\left(hf_r/2k_BT\right)}{\left(1+\langle n\rangle/n_c\right)^{\beta}} + \delta_0. \qquad \text{(E1)}$$

Here, the first term contains the power dependence and relates to the TLS. Specifically, the imaginary part of the TLS susceptibility is accounted for here and resembles a Lorentzian function [33] so that the loss arises from TLS that are spectrally close to the resonator. In this model, n_c is the number of photons equivalent to the saturation field of one TLS, F is the filling factor, which is the ratio of electric field threading the TLS to the total electric field. Collectively, $F\delta^0_{\mathrm{TLS}}$ gives the TLS loss, where, assuming TLS of predominantly similar dipole moments, δ^0_{TLS} describes a density of TLS.

Recent results have demonstrated that TLS are not spectrally stable [32,41,58,59], which results in a time-varying

TABLE III. Nanowire superinductance resonator parameters of five devices. $F\delta^0_{\mathrm{TLS}}$ and β are obtained from fits to Eq. (E1), $F\delta^i_{\mathrm{TLS}}$ from fits to Eq. (2) of the main text, and finally P_γ from fits to Eq. (3).

NW f_r (MHz)	β	$F\delta^0_{\mathrm{TLS}}$ ($\times10^{-5}$)	$F\delta^i_{\mathrm{TLS}}$ ($\times10^{-5}$)	P_γ
4420	0.198	8.81	4.37	0.195
4562	0.196	7.51	3.84	0.183
4685	0.187	10.7	3.53	0.218
4837	0.180	8.24	4.40	0.153
5285	0.184	10.8	4.12	0.213

number of near-resonant TLS that is revealed as a time-varying quality factor [37]. In the context of the TLS loss model, this spectral instability of the TLS means that the TLS spends less time resonant with the resonator. Consequently, the TLS is not always present as a loss channel to the resonator, which motivates a weaker power dependence of the TLS loss term. In the above, β describes the strength of TLS saturation with power and the original TLS model predicts $\beta = 0.5$ [43]. However, due to the spectral instability of TLS, recent results [26,32,40,44] commonly find a weaker scaling. Therefore, we allow β to be a fit parameter initialized to $\beta = 0.5$ and we find that $\beta \simeq 0.2$ best describes our data (see Table III). Rather than allowing β to be a fit parameter, Faoro and Ioffe [41] showed that the spectral instability of TLS results in the microwave-power dependence of the dielectric loss becoming logarithmic. This is the model we use in the main text to fit our data, and it is given by

$$\frac{1}{Q_i} = F\delta^i_{\mathrm{TLS}}P_\gamma\ln\left(\frac{cn_c}{\langle n\rangle} + \delta_0'\right)\tanh\left(\frac{hf_r}{2k_BT}\right). \qquad \text{(E2)}$$

Here, F is once again the filling factor and δ^i_{TLS} is the intrinsic TLS loss tangent. Additionally, P_γ is the TLS switching rate ratio, defined by $P_\gamma = 1/\ln(\gamma_{\max}/\gamma_{\min})$ where $\gamma_{\max}$ and $\gamma_{\min}$ are the maximum and minimum rate of TLS switching, respectively, c is a large constant, n_c is the number of photons generating the electric field saturating a TLS, and δ_0' is the log-scaled next dominant loss rate. The temperature-dependent hyperbolic tangent scaling highlights the thermal saturation of TLS. As shown in the main text, this model describes our data well and the obtained fitted values are in good agreement with other results [40,43,44].

The intrinsic loss tangent δ^i_{TLS} used above is obtained, by means of the Kramers-Kronig relation via the real component of the TLS susceptibility, by measuring the $f_r(T)$ using the PFLL. Measuring the real component is preferable for a variety of reasons: fundamentally, it scales more slowly vs frequency [33], making it more robust to the spectral instability of TLS. Another factor is simply that measuring frequency is significantly more accurate than measuring quality factors. Additionally, we note that $F\delta^0_{\mathrm{TLS}}$

and $F\delta^{i}_{\mathrm{TLS}}$ differ by a factor 2 to 3, which is significantly larger than the approximately 15% difference typically observed [26]. However, this is not unexpected, as the low value of β indicated that we are outside of the range of validity of Eq. (E1) [26,40].

[1] E. F. C. Driessen, P. C. J. J. Coumou, R. R. Tromp, P. J. de Visser, and T. M. Klapwijk, Strongly Disordered TiN and NbTiN *s*-Wave Superconductors Probed by Microwave Electrodynamics, Phys. Rev. Lett. **109**, 107003 (2012).

[2] Mintu Mondal, Anand Kamlapure, Madhavi Chand, Garima Saraswat, Sanjeev Kumar, John Jesudasan, L. Benfatto, Vikram Tripathi, and Pratap Raychaudhuri, Phase Fluctuations in a Strongly Disordered *s*-Wave NbN Superconductor Close to the Metal-Insulator Transition, Phys. Rev. Lett. **106**, 047001 (2011).

[3] Y. Noat, V. Cherkez, C. Brun, T. Cren, C. Carbillet, F. Debontridder, K. Ilin, M. Siegel, A. Semenov, H.-W. Huübers, and D. Roditchev, Unconventional superconductivity in ultrathin superconducting NbN films studied by scanning tunneling spectroscopy, Phys. Rev. B **88**, 014503 (2013).

[4] O. V. Astafiev, L. B. Ioffe, S. Kafanov, Yu A. Pashkin, K. Yu Arutyunov, D. Shahar, O. Cohen, and J. S. Tsai, Coherent quantum phase slip, Nature **484**, 355 (2012).

[5] D. B. Haviland, Y. Liu, and A. M. Goldman, Onset of Superconductivity in the Two-Dimensional Limit, Phys. Rev. Lett. **62**, 2180 (1989).

[6] Nicholas A. Masluk, Ioan M. Pop, Archana Kamal, Zlatko K. Minev, and Michel H. Devoret, Microwave Characterization of Josephson Junction Arrays: Implementing a Low Loss Superinductance, Phys. Rev. Lett. **109**, 137002 (2012).

[7] M. T. Bell, I. A. Sadovskyy, L. B. Ioffe, A. Yu Kitaev, and M. E. Gershenson, Quantum Superinductor with Tunable Nonlinearity, Phys. Rev. Lett. **109**, 137003 (2012).

[8] Vladimir E. Manucharyan, Jens Koch, Leonid I. Glazman, and Michel H. Devoret, Fluxonium: Single Cooper-pair circuit free of charge offsets, Science **326**, 113 (2009).

[9] Ioan M. Pop, Kurtis Geerlings, Gianluigi Catelani, Robert J. Schoelkopf, Leonid I. Glazman, and Michel H. Devoret, Coherent suppression of electromagnetic dissipation due to superconducting quasiparticles, Nature **508**, 369 (2014).

[10] Andrew J. Kerman, Metastable Superconducting Qubit, Phys. Rev. Lett. **104**, 027002 (2010).

[11] F. Luthi, T. Stavenga, O. W. Enzing, A. Bruno, C. Dickel, N. K. Langford, M. A. Rol, T. S. Jespersen, J. Nygård, P. Krogstrup, and L. DiCarlo, Evolution of Nanowire Transmon Qubits and their Coherence in a Magnetic Field, Phys. Rev. Lett. **120**, 100502 (2018).

[12] N. Samkharadze, G. Zheng, N. Kalhor, D. Brousse, A. Sammak, U. C. Mendes, A. Blais, G. Scappucci, and L. M. K. Vandersypen, Strong spin-photon coupling in silicon, Science **359**, 1123 (2018).

[13] N. Samkharadze, A. Bruno, P. Scarlino, G. Zheng, D. P. DiVincenzo, L. DiCarlo, and L. M. K. Vandersypen, High-Kinetic-Inductance Superconducting Nanowire Resonators for Circuit QED in a Magnetic Field, Phys. Rev. Appl. **5**, 044004 (2016).

[14] A. Stockklauser, P. Scarlino, J. V. Koski, S. Gasparinetti, C. K. Andersen, C. Reichl, W. Wegscheider, T. Ihn, K. Ensslin, and A. Wallraff, Strong Coupling Cavity QED with Gate-Defined Double Quantum Dots Enabled by a High Impedance Resonator, Phys. Rev. X **7**, 011030 (2017).

[15] A. J. Landig, J. V. Koski, P. Scarlino, U. C. Mendes, A. Blais, C. Reichl, W. Wegscheider, A. Wallraff, K. Ensslin, and T. Ihn, Coherent spin-photon coupling using a resonant exchange qubit, Nature **560**, 179 (2018).

[16] J. J. Viennot, M. C. Dartiailh, A. Cottet, and T. Kontos, Coherent coupling of a single spin to microwave cavity photons, Science **349**, 408 (2015).

[17] Jiansong Gao, Miguel Daal, Anastasios Vayonakis, Shwetank Kumar, Jonas Zmuidzinas, Bernard Sadoulet, Benjamin A. Mazin, Peter K. Day, and Henry G. Leduc, Experimental evidence for a surface distribution of two-level systems in superconducting lithographed microwave resonators, Appl. Phys. Lett. **92**, 152505 (2008).

[18] W. Guichard and F. W. J. Hekking, Phase-charge duality in Josephson junction circuits: Role of inertia and effect of microwave irradiation, Phys. Rev. B **81**, 064508 (2010).

[19] Peter Brooks, Alexei Kitaev, and John Preskill, Protected gates for superconducting qubits, Phys. Rev. A **87**, 052306 (2013).

[20] Andrey Belkin, Matthew Brenner, Thomas Aref, Jaseung Ku, and Alexey Bezryadin, Little–Parks oscillations at low temperatures: Gigahertz resonator method, Appl. Phys. Lett. **98**, 242504 (2011).

[21] J. T. Peltonen, O. V. Astafiev, Yu P. Korneeva, B. M. Voronov, A. A. Korneev, I. M. Charaev, A. V. Semenov, G. N. Golt'sman, L. B. Ioffe, T. M. Klapwijk, and J. S. Tsai, Coherent flux tunneling through NbN nanowires, Phys. Rev. B **88**, 220506 (2013).

[22] J. T. Peltonen, Z. H. Peng, Yu P. Korneeva, B. M. Voronov, A. A. Korneev, A. V. Semenov, G. N. Gol'tsman, J. S. Tsai, and O. V. Astafiev, Coherent dynamics and decoherence in a superconducting weak link, Phys. Rev. B **94**, 180508 (2016).

[23] J. T. Peltonen, P. C. J. J. Coumou, Z. H. Peng, T. M. Klapwijk, J. S. Tsai, and O. V. Astafiev, Hybrid rf squid qubit based on high kinetic inductance, Sci. Rep. **8**, 10033 (2018).

[24] P. C. J. J. Coumou, M. R. Zuiddam, E. F. C. Driessen, P. J. de Visser, J. J. A. Baselmans, and T. M. Klapwijk, Microwave properties of superconducting atomic-layer deposited tin films, IEEE T. Appl. Supercon. **23**, 7500404 (2013).

[25] M. V. Feigel'man and L. B. Ioffe, Microwave Properties of Superconductors Close to the Superconductor-Insulator Transition, Phys. Rev. Lett. **120**, 037004 (2018).

[26] J. Burnett, J. Sagar, O. W. Kennedy, P. A. Warburton, and J. C. Fenton, Low-Loss Superconducting Nanowire Circuits using a Neon Focused Ion Beam, Phys. Rev. Appl. **8**, 014039 (2017).

[27] S. Probst, F. B. Song, P. A. Bushev, A. V. Ustinov, and M. Weides, Efficient and robust analysis of complex scattering data under noise in microwave resonators, Rev. Sci.Instrum. **86**, 024706 (2015).

[28] M. Tinkham, *Introduction to Superconductivity* (Dover Books, Mineola, NY, 2004).

[29] S. S. Mohan, M. del Mar Hershenson, S. P. Boyd, and T. H. Lee, Simple accurate expressions for planar spiral inductances, IEEE J. Solid-St. Circ. **34**, 1419 (1999).

[30] L. J. Swenson, P. K. Day, B. H. Eom, H. G. Leduc, N. Llombart, C. M. McKenney, O. Noroozian, and J. Zmuidzinas, Operation of a titanium nitride superconducting microresonator detector in the nonlinear regime, J. Appl. Phys. **113**, 104501 (2013).

[31] K. D. Osborn, J. A. Strong, A. J. Sirois, and R. W. Simmonds, Frequency-tunable Josephson junction resonator for quantum computing, IEEE T. Appl. Supercond. **17**, 166 (2007).

[32] J. Burnett, L. Faoro, I. Wisby, V. L. Gurtovoi, A. V. Chernykh, G. M. Mikhailov, V. A. Tulin, R. Shaikhaidarov, V. Antonov, P. J. Meeson, A. Ya Tzalenchuk, and T. Lindström, Evidence for interacting two-level systems from the 1/f noise of a superconducting resonator, Nat. Commun. **5**, 4119 (2014).

[33] D. P. Pappas, M. R. Vissers, D. S. Wisbey, J. S. Kline, and J. Gao, Two level system loss in superconducting microwave resonators, IEEE T. Appl. Supercond. **21**, 871 (2011).

[34] Christian Enss and Siegfried Hunklinger, *Low-Temperature Physics* (Springer-Verlag, Berlin, Heidelberg, 2005).

[35] P. Macha, S. H. W. van der Ploeg, G. Oelsner, E. Ilichev, H.-G. Meyer, S. Wünsch, and M. Siegel, Losses in coplanar waveguide resonators at millikelvin temperatures, Appl. Phys. Lett. **96**, 062503 (2010).

[36] G. Calusine, A. Melville, W. Woods, R. Das, C. Stull, V. Bolkhovsky, D. Braje, D. Hover, D. K. Kim, X. Miloshi, D. Rosenberg, A. Sevi, J. L. Yoder, E. Dauler, and W. D. Oliver, Analysis and mitigation of interface losses in trenched superconducting coplanar waveguide resonators, Appl. Phys. Lett. **112**, 062601 (2018).

[37] C. T. Earnest, J. H. Beéjanin, T. G. McConkey, E. A. Peters, A. Korinek, H. Yuan, and M. Mariantoni, Substrate surface engineering for high-quality silicon/aluminum superconducting resonators, Supercond. Sci. Technol. **31**, 125013 (2018).

[38] Jürgen Lisenfeld, Grigorij J. Grabovskij, Clemens Müller, Jared H. Cole, Georg Weiss, and Alexey V. Ustinov, Observation of directly interacting coherent two-level systems in an amorphous material, Nat. Commun. **6**, 6182 (2015).

[39] Lara Faoro and Lev B. Ioffe, Internal Loss of Superconducting Resonators Induced by Interacting Two-Level Systems, Phys. Rev. Lett. **109**, 157005 (2012).

[40] S. E. de Graaf, L. Faoro, J. Burnett, A. A. Adamyan, A. Ya Tzalenchuk, S. E. Kubatkin, T. Lindstroöm, and A. V. Danilov, Suppression of low-frequency charge noise in superconducting resonators by surface spin desorption, Nat. Commun. **9**, 1143 (2018).

[41] Lara Faoro and Lev B. Ioffe, Interacting tunneling model for two-level systems in amorphous materials and its predictions for their dephasing and noise in superconducting microresonators, Phys. Rev. B **91**, 014201 (2015).

[42] S. Kafanov, H. Brenning, T. Duty, and P. Delsing, Charge noise in single-electron transistors and charge qubits may be caused by metallic grains, Phys. Rev. B **78**, 125411 (2008).

[43] J. Burnett, L. Faoro, and T. Lindström, Analysis of high quality superconducting resonators: Consequences for TLS properties in amorphous oxides, Supercond. Sci. Tech. **29**, 044008 (2016).

[44] Naftali Kirsh, Elisha Svetitsky, Alexander L. Burin, Moshe Schechter, and Nadav Katz, Revealing the nonlinear response of a tunneling two-level system ensemble using coupled modes, Phys. Rev. Mat. **1**, 012601 (2017).

[45] R. Barends, H. L. Hortensius, T. Zijlstra, J. J. A. Baselmans, S. J. C. Yates, J. R. Gao, and T. M. Klapwijk, Contribution of dielectrics to frequency and noise of NbTiN superconducting resonators, Appl. Phys. Lett. **92**, 223502 (2008).

[46] Y. Chen, H. Yang, and Z. Cui, Effects of developing conditions on the contrast and sensitivity of hydrogen silsesquioxane, Microelect. Eng. **83**, 1119 (2006).

[47] Gerd Bergmann, Physical interpretation of weak localization: A time-of-flight experiment with conduction electrons, Phys. Rev. B **28**, 2914 (1983).

[48] J. E. Mooij, *Percolation, Localization and Superconductivity* (Plenum Press, New York, NY, 1984).

[49] T. Lindström, J. E. Healey, M. S. Colclough, C. M. Muirhead, and A. Ya Tzalenchuk, Properties of superconducting planar resonators at millikelvin temperatures, Phys. Rev. B **80**, 132501 (2009).

[50] R. V. Pound, Electronic frequency stabilization of microwave oscillators, Rev. Sci. Instrum. **17**, 490 (1946).

[51] Eric D. Black, An introduction to Pound–Drever–Hall laser frequency stabilization, Am. J. Phys. **69**, 79 (2001).

[52] T. Lindström, J. Burnett, M. Oxborrow, and A. Ya Tzalenchuk, Pound-locking for characterization of superconducting microresonators, Rev. Sci. Instrum. **82**, 104706 (2011).

[53] S. E. de Graaf, A. V. Danilov, A. Adamyan, T. Bauch, and S. E. Kubatkin, Magnetic field resilient superconducting fractal resonators for coupling to free spins, J. Appl. Phys. **112**, 123905 (2012).

[54] M. H. Devoret, Steven Girvin, and Robert Schoelkopf, Circuit-QED: How strong can the coupling between a Josephson junction atom and a transmission line resonator be? Ann. Phys. **16**, 767 (2007).

[55] Yachin Ivry, Chung-Soo Kim, Andrew E. Dane, Domenico De Fazio, Adam N. McCaughan, Kristen A. Sunter, Qingyuan Zhao, and Karl K. Berggren, Universal scaling of the critical temperature for thin films near the superconducting-to-insulating transition, Phys. Rev. B **90**, 214515 (2014).

[56] J. Gao, Ph.D. thesis, School California Institute of Technology, 2008.

[57] Daniel F. Santavicca, Jesse K. Adams, Lierd E. Grant, Adam N. McCaughan, and Karl K. Berggren, Microwave dynamics of high aspect ratio superconducting nanowires studied using self-resonance, J. Appl. Phys. **119**, 234302 (2016).

[58] Clemens Müller, Jürgen Lisenfeld, Alexander Shnirman, and Stefano Poletto, Interacting two-level defects as sources of fluctuating high-frequency noise in superconducting circuits, Phys. Rev. B **92**, 035442 (2015).

[59] P. V. Klimov *et al.*, Fluctuations of Energy-Relaxation Times in Superconducting Qubits, Phys. Rev. Lett. **121**, 090502 (2018).